Application of Model-Free Control to Reduce the Total Harmonic Distortion of Inverters

Jan Wachter, Lutz Gröll and Veit Hagenmeyer
Institute for Automation and Applied Informatics
Karlsruhe Institute of Technology (KIT) Karlsruhe, Germany
jan.wachter@kit.edu

***Abstract*—With the fast rising number of power electronic devices in the electric grid, the harmonic emissions of those devices can lead to significant power quality issues. This is reflected in the recent addition of harmonic stability as one of the grid stability types. The reduction of harmonic emissions is an important task in the development of resilient carbon neutral grids. This paper describes the application of the model-free control concept for grid-tied inverters as an easily implementable extension for dq0-frame based current control loops, which are often used in cascaded control schemes. The approach incorporates the information contained in the output current derivative. To balance phase-error and measurement noise suppression, the derivative is obtained using an algebraic numerical differentiator. The reduction of the total harmonic distortion (THD) is demonstrated for two use-cases in simulation, in order to show the transferability of the results. Further, measurement data from a hardware implementation of the concept is studied to verify the behavior under real-world conditions. For this, the influence of the tuning parameters is discussed along with limitations of the approach.**

***Index Terms*—power electronics, model-free control, total harmonic distortion**

I. Introduction

The transition of the power system towards a sustainable system affects all layers of the power grid. A major development is the increasing penetration of power electronically interfaced devices. Due to the switching nature of power electronic devices, they inherently introduce (inter-)harmonic frequency components in the grid [1]. Such non-base frequency oscillations can interact with each other or with the power grid and lead to severe power quality issues by exciting resonances as described in real-world studies [2]–[6]. Further, the importance of this development is reflected in the recent extension of the IEEE power grid stability definitions by the category of converter-driven stability, that includes harmonic stability [7].

The amount of harmonic content emissions is influenced by various factors, such as the grid connection filters and the control system. Changes that concern hardware come always with additional costs. Therefore the use of software or control solutions to reduce harmonic emissions of grid connected devices is favorable and holds high potential, especially in the case of mitigating problems after commissioning by updating the control software [8]. Model based control approaches to reduce the harmonic content, cf. [9] and the references within, rely on the knowledge of system parameters. This is unfavorable for real-world applications, since the grid environment is usually not exactly known and mass produced converters have production tolerances that need to be accounted for. The concept of model-free control [10] can be deployed to compensate parametric as well as ambient uncertainties. Recent application of related concepts for power electronics include: power control for rectifiers [11] or the predictive sliding mode control of voltage source inverters in [12]. In these applications the reduction of current ripples and/or total harmonic distortion (THD) is reported.

The present paper details how the idea of model-free control can be understood as an add-on for dq0-frame based current controllers, allowing to retain the tuning and structure of existing cascaded control schemes and have a THD reducing effect. This is shown for two simulation examples: (i) simulation replica of the later used hardware testbench of an inverter system and (ii) a simulink example system of a power electronically interfaced microturbine. Furthermore, the simulation results are verified by hardware experiments of a grid-tied, three-phase inverter system.

The remainder of this paper is structured as follows. Section II gives a brief overview of the system under study and derives the model equations which are used to motivate the design of the baseline current controller. Afterwards in Sec. III the concept of model-free control is briefly described and the application to the current control loop of an inverter system is detailed. Section IV provides and discusses the simulation results. Afterwards in Sec. V, the experimental setup is described and the measurement results are presented. Further the influence of the tuning parameters of the approach is discussed, along with limitations of the implementation. Lastly, Sec. VI summarizes the findings and concludes the paper.

II. System under Study and baseline current control scheme

A. Three-phase inverter model

In the following, the model equations for the considered grid-tied three-phase inverters are derived, see Fig. 1 for the electric scheme of the considered system. The following assumptions are made:

- *Well regulated DC-link:* Assuming a constant source voltage V_{dc} and well sized DC-link capacitors, we neglect the DC-link dynamics.

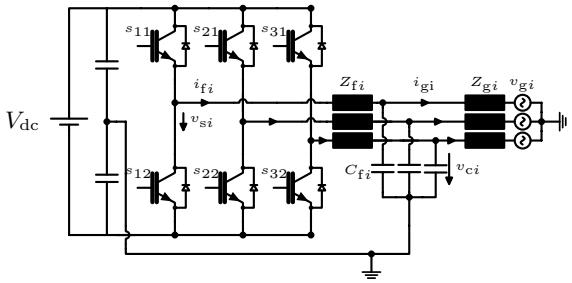

Fig. 1: Schematics of the two level inverter which is interfaced with a LC filter to the grid, the index i is used for the per-phase parameters and signals. The filter and grid impedance are given by $Z_{\mathrm{f}i} = R_{\mathrm{f}i} + j\, L_{\mathrm{f}i}$ and $Z_{\mathrm{g}i} = R_{\mathrm{g}i} + j\, L_{\mathrm{g}i}$.

- *Ideal switches and averaging:* Furthermore, we assume averaging over one PWM carrier period for all physical signals, such that averaging justifies using the modulation signal m_i for each of the phases instead of the gate signals s_{ij}. Moreover, all switching losses and parasitic effects are neglected.
- *Ideal, symmetric passive components:* The passive components are assumed to be symmetric, such that the phase index is neglected in the following. Furthermore, all unmodeled parasitic and non-linear effects are neglected.

This yields the average model

$$\frac{\mathrm{d}i_{\mathrm{f}i}}{\mathrm{d}t} = \frac{1}{L_{\mathrm{f}}}\left(-v_{ci} - R_{\mathrm{L_f}} i_{\mathrm{f}i} + \frac{1}{2} V_{\mathrm{dc}} m_i\right), \tag{1}$$

$$\frac{\mathrm{d}v_{ci}}{\mathrm{d}t} = \frac{1}{C_{\mathrm{f}}}\left(i_{\mathrm{f}i} - i_{\mathrm{g}i}\right), \tag{2}$$

$$\frac{\mathrm{d}i_{\mathrm{g}i}}{\mathrm{d}t} = \frac{1}{L_{\mathrm{g}}}\left(v_{ci} - v_{\mathrm{g}i} - R_{\mathrm{g}} i_{\mathrm{g}i}\right), \tag{3}$$

where $i_{\mathrm{f}i}$ and $i_{\mathrm{g}i}$ are the currents through the filter inductance and into the grid, respectively. The grid voltage is denoted by $v_{\mathrm{g}i}$, the grid inductance and resistance by $L_{\mathrm{g}i}$ and $R_{\mathrm{g}i}$, respectively. Furthermore, L_{f}, $R_{\mathrm{L_f}}$ and C_{f} represent the filter inductance, parasitic inductor resistance and capacitance, and $v_{\mathrm{c}i}$ the filter capacitor voltage. The switched voltage of the inverter output is given by $v_{\mathrm{s}i} = \frac{1}{2} V_{\mathrm{dc}}\, m_i$, where m_i from the interval $(-1, 1)$ is the modulation signal of the corresponding PWM controlled switches.

B. Baseline current control scheme

To motivate the typical structure of current controllers, cf. [13], we consider the filter current dynamics given in (1). First we obtain the filter currents in dq0-coordinates i_{dq0} via the Park transformation $\mathcal{P}(\theta_{\mathrm{g}})$ [14], which is given as

$$\mathcal{P}(\theta_{\mathrm{g}}) = \frac{2}{3}\begin{bmatrix} \cos(\theta_{\mathrm{g}}) & \cos(\theta_{\mathrm{g}} - \frac{2\pi}{3}) & \cos(\theta_{\mathrm{g}} + \frac{2\pi}{3}) \\ -\sin(\theta_{\mathrm{g}}) & -\sin(\theta_{\mathrm{g}} - \frac{2\pi}{3}) & -\sin(\theta_{\mathrm{g}} + \frac{2\pi}{3}) \\ \frac{1}{2} & \frac{1}{2} & \frac{1}{2} \end{bmatrix},$$

where θ_{g} is the grid voltage angle, for example obtained by a phase-locked loop (PLL) system. This yields for the filter currents $i_{\mathrm{dq0}} = \mathcal{P}(\theta_{\mathrm{g}})\, i_{abc}$, where $i_{abc} = \begin{bmatrix} i_{\mathrm{f}_1} & i_{\mathrm{f}_2} & i_{\mathrm{f}_3} \end{bmatrix}^\top$ denotes the filter current vector in abc-coordinates.
To obtain the dynamics of i_{dq0}, we start from

$$\frac{\mathrm{d}i_{\mathrm{abc}}}{\mathrm{d}t} = \frac{\mathrm{d}}{\mathrm{d}t}(\mathcal{P}^{-1}(\theta_{\mathrm{g}})\, i_{\mathrm{dq0}}). \tag{4}$$

Using the product rule and left multiplication of $\mathcal{P}(\theta_{\mathrm{g}})$ yields

$$\frac{\mathrm{d}i_{\mathrm{dq0}}}{\mathrm{d}t} = -\mathcal{P}(\theta_{\mathrm{g}})\, \frac{\mathrm{d}\mathcal{P}^{-1}(\theta_{\mathrm{g}})}{\mathrm{d}t}\, i_{\mathrm{dq0}} + \mathcal{P}(\theta_{\mathrm{g}})\, \frac{\mathrm{d}i_{\mathrm{abc}}}{\mathrm{d}t}, \tag{5}$$

for which we use the relation [14]

$$\frac{\mathrm{d}\mathcal{P}^{-1}(\theta_{\mathrm{g}})}{\mathrm{d}t} = \mathcal{P}^{-1}(\theta_{\mathrm{g}})\, \mathcal{D}(\dot{\theta}_{\mathrm{g}}), \tag{6}$$

where

$$\mathcal{D}(\dot{\theta}_{\mathrm{g}}) = \begin{bmatrix} 0 & -\dot{\theta}_{\mathrm{g}} & 0 \\ \dot{\theta}_{\mathrm{g}} & 0 & 0 \\ 0 & 0 & 0 \end{bmatrix}.$$

If the grid is operating close to its nominal frequency, we can assume $\dot{\theta}_{\mathrm{g}} = \omega_{\mathrm{g,\,nom}}$. Inserting (1) and (6) in (5), and further defining the control input $u := \frac{1}{2} V_{\mathrm{dc}} m_{\mathrm{dq0}}$ yields

$$\frac{\mathrm{d}i_{\mathrm{dq0}}}{\mathrm{d}t} = \mathcal{D}(\omega_{\mathrm{g,\,nom}})\, i_{\mathrm{dq0}} + \frac{1}{L_{\mathrm{f}}}\left(-v_{\mathrm{c},dq0} - R_{\mathrm{L_f}} i_{\mathrm{dq0}} + u\right).$$

The term $R_{\mathrm{L_f}} i_{\mathrm{dq0}}$ can be neglected because the typical values of the parasitic resistance $R_{\mathrm{L_f}}$ are small compared to the other terms. With $e = (i_{\mathrm{dq0,d}} - i_{\mathrm{dq0}})$ representing the deviation from the current setpoint $i_{\mathrm{dq0,d}}$, it is easy to see that it makes sense to close the loop with a controller of the form

$$u = \underbrace{-L_{\mathrm{f}}\, \mathcal{D}(\omega_{\mathrm{g,\,nom}})\, i_{\mathrm{dq0}}}_{\text{decoupling}} + \underbrace{v_{\mathrm{c},dq0}}_{\text{voltage-ff}} + \underbrace{k_p\, e + k_i \int e\, \mathrm{d}\tau}_{\text{PI controller}},$$

where k_p, k_i are the gains of the proportional-integral (PI) controller. Note that the 0-axis is often neglected, since the zero component is zero under balanced grid conditions. This uncovers the typical components of current control schemes, cf. [13]: (i) decoupling network for the dq-axis inductor currents (decoupling), (ii) feedforward of the capacitor voltage (voltage-ff), (iii) PI controller for the dq-axis.
Remark: As is clear from the considerations above, several dynamics of the system are not considered in the design. It is well known from practice, that harmonic distortions are always present to some extend in real systems and can stem from various sources, e.g. distortions of the grid voltage or non-linear behavior of components. Considering (2) and (3), we see that such unconsidered dynamics interact directly with the filter current. This motivates using the information contained in these dynamics to improve the control performance, as detailed in the next section.

III. Model-free control for the inverter system

A. Brief overview of model-free control

The central idea of the model-free control approach [10] is leveraging an ultra-local model which is expressed as

$$y^{(\nu)} = F + \alpha\, \tilde{u}, \tag{7}$$

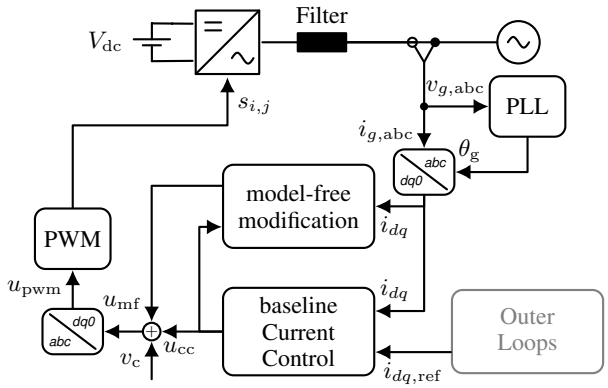

Fig. 2: Scheme of the model-free controller as a baseline current controller and model-free modification for the inverter system.

where $y^{(\nu)}$ is the ν^{th}-derivative of the output y, F contains all the uncertain, unknown, or lumped system dynamics, α is a non-physical tuning parameter and $\tilde{u}$ the control input of the plant. The value of F is estimated and updated by a suitable approach. For this, the ultra-local model is used to obtain the control law. Assuming $\nu = 1$ and using (7), it can be written as

$$\tilde{u} = -\frac{F - \dot{y}_{\mathrm{d}} + \zeta(e)}{\alpha}\,, \tag{8}$$

where $\zeta(e)$ is a causal functional of the control deviation e, and y_{d} the desired output. For the current control for inverters, we already have reliably tuned PI controllers that we can use as $\zeta(e)$. In this setting we can interpret (8) to consist of a baseline controller (BLC) and a model-free modification (MFM)

$$\tilde{u} = -\underbrace{\frac{F - \dot{y}_{\mathrm{d}}}{\alpha}}_{\mathrm{MFM}} - \underbrace{\frac{\zeta(e)}{\alpha}}_{\mathrm{BLC}}\,. \tag{9}$$

The schematics of the resulting structure are shown in Fig. 2. Due to the incorporation of additional information in the control law, which is contained in F the control performance is expected to improve. Furthermore, the well-known properties of the PI baseline controller are preserved. This of course depends on the obtainability and quality of F.

B. Application of model-free control to the current controller of an inverter system

In this section we consider the application of the model-free control approach to the current control loop of an inverter as shown in Fig. 1. The output of the ultra-local model, y in (7), is defined as as the filter currents in dq0-coordinates i_{dq0}. Furthermore, the input is chosen as u_{cc} (PI controller including decoupling) as depicted in Fig. 2. This yields the following for the ultra-local model

$$F = \frac{\mathrm{d}i_{\mathrm{dq0}}}{\mathrm{d}t} - \alpha\, u_{\mathrm{cc}}\,. \tag{10}$$

From an implementation point of view, the derivative of i_{dq0} is the only signal that is not directly available, it must be calculated. Since the measured currents are subject to significant noise, suitable approaches must be used to ensure an acceptable signal to noise ratio. For this, derivative-free online-identification methods are proposed in [10] and the application reference therein, or assumptions are used as in [12] to avoid differentiation of noisy signals. For the present application we use algebraic numerical differentiators, cf. [15] for an extensive survey. For such derivative-free differentiators, the derivative estimate can be expressed as [15]

$$\hat{y}^{(n)}(t) = \int_0^T g_T^{(n)}(\tau) y(t-\tau)\,\mathrm{d}\tau\,,$$

with the filter length T. The filter kernel g_T has the form

$$g_T(t) = \frac{2}{T}\sum_{i=0}^{N} \frac{P_i^{(\alpha_d,\beta_d)}(\nu(t))}{\left\|P_i^{(\alpha_d,\beta_d)}\right\|^2} w^{(\alpha_d,\beta_d)}\left(\nu(t)\right) P_i^{(\alpha_d,\beta_d)}\left(\nu(t)\right),$$

with $P_i^{(\alpha_d,\beta_d)}$ being Jacobi polynomials and $\nu(t) = 1 - \frac{2}{T}t$. The norm $\left\|x\right\| = \sqrt{\langle x, x\rangle}$ is induced by the inner product

$$\langle x, y\rangle = \int_{-1}^{1} w^{(\alpha_d,\beta_d)}(\tau) x(\tau) y(\tau)\mathrm{d}\tau,$$

where $\omega^{(\alpha_d,\beta_d)}$ is the weight function

$$w^{(\alpha,\beta)}(\tau) = \begin{cases} (1-\tau)^{\alpha_d}(1+\tau)^{\beta_d}, & \tau \in [-1,1], \\ 0, & \text{otherwise.} \end{cases}$$

The behavior of the resulting filter is determined by:

- Degree of the polynomial N, that approximates the signal $y^{(n)}$
- Filter length T, which can be computed from a desired cutoff-frequency $\omega_{c,\mathrm{d}}$
- Weight function parameters α_d and β_d

For the implementation, we leverage the fact that such differentiators can be discretized and implemented as finite impulse response (FIR) filters. Using the above mentioned parameters, the python toolbox[1] described in [15] is used to design the FIR filter for the current derivative. The chosen parameters are described in the following sections for each of the applications. To attenuate unwanted high frequency components in the resulting signal due to measurement noise, a first-order low pass filter (LPF) with a static gain of one is implemented as shown in the signal flow chart of the MFM, cf. Figure 3. Note that the current implementation uses the same α for all axes of the dq0-system.

IV. Simulation Results

In this section two simulation examples are considered. One is the simulation replica of the later used hardware testbench, and the other a simulink example model[2] of a three-phase inverter that connects a microturbine to the grid. The latter

[1] https://github.com/aothmane-control/Algebraic-differentiators

[2] https://de.mathworks.com/help/sps/ug/two-level-pwm-converter-and-dead-time.html

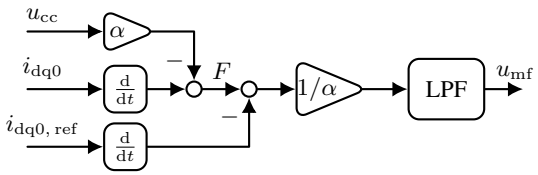

Fig. 3: Scheme of the model-free control modification.

TABLE I: Parameter values of the testbench simulation and hardware setup.

Parameter	Value	Description
V_g	230 V	grid RMS voltage
f_g	50 Hz	grid nominal frequency
f_s	20 kHz	sampling frequency
f_c	20 kHz	control cycle frequency
L_g	400 μH	grid inductance
R_g	0.05 Ω	grid resistance
L_f	2.3 mH	filter inductance
C_f	10 μF	filter capacitor
V_{dc}	750 μV	dc-link voltage

example is chosen to show the transferability of the approach to similar power electronic systems.

A. Testbench simulation results and discussion

The simulations are carried out with a simulation replica of the hardware testbench, see Fig. 1 and 7. Table I, summarizes the parameters of the inverter and its environment. All testbench components are modeled using the simulink specialized power-systems library[3], the three-phase inverter is modeled as a switched system. Measurement noise is added to the grid current measurement as band-limited white noise to increase realism. The grid is modeled as an ideal three-phase voltage source and the connecting power line as a series resistance and inductance. All default control parameters are given in Tab. II, deviations are noted where applicable.

Figure 2 shows the control system of the inverter, no outer loops are used in this example. For the baseline experiment, only the reference PI controller is used, cf. Fig. 2 with disabled model-free modification (MFM). The inverter is connected to the grid and a current setpoint of $i_{dq,\,d} = [5 \quad 0]^\top$ is applied.

[3]https://de.mathworks.com/help/sps/specialized-power-systems.html

TABLE II: Control parameters used for the testbench simulation and hardware setup

Parameter	Value	Description
$\omega_{c,\,d}$	$3000\pi\,\frac{rad}{s}$	cutoff frequency derivative-filter
α_d	2	derivative filter parameter
β_d	2	derivative filter parameter
N	2	derivative filter polynominal order
$\omega_{c,\,lpf}$	$2000\pi\,\frac{rad}{s}$	cutoff frequency LPF
α	700	tuning parameter of the controller
k_p	5	current-controller proportional gain
k_i	240	current-controller integral gain

During steady state a 3 s sample of the filter current is taken to evaluate the THD, which is defined as the ratio of the root mean square (RMS) value of the harmonic content to the fundamental component expressed in percent [16]. This yields

$$\mathrm{THD} = 100\,\% \frac{\sqrt{\sum_{j=2}^{n} I_j^2}}{I_\mathrm{f}}, \tag{11}$$

where I_j represent the RMS value of the j^{th} current harmonic and I_f the RMS value of the nominal frequency current. For different scenarios of the testbench simulation the THD is reduced between 21.2 % to 24.3 %, depending on the used cutoff frequency of the LPF. This shows that the MFM exhibits the desired behavior in the provided simulation example. The attenuation of the individual harmonics is presented in Fig. 4, the comparison between PI baseline and enabled MFM clearly shows that the content of the lower harmonics is decreased. The testbench simulation is used to discuss the influence of

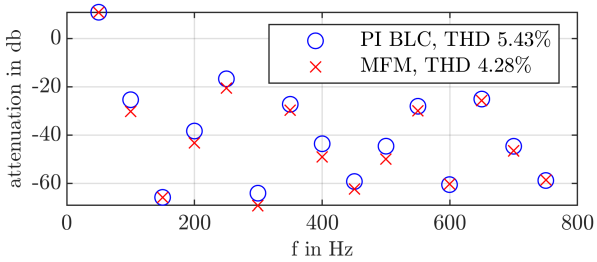

Fig. 4: Comparison of the attenuation of the lower harmonics with enabled MFM, for $\alpha = 700$ and $\omega_{c,\mathrm{lpf}} = 2000\pi\,\frac{rad}{s}$.

the LPF used to suppress higher frequencies introduced by measurement noise and the derivative action. The results for different cutoff frequencies of the LPF $\omega_{c,\mathrm{lpf}}$ are shown in Tab. III. Clearly, a smaller cut off frequency reduces the effect

TABLE III: Influence of LPF cutoff frequency on the THD for enabled MFM with $\alpha = 700$ in the testbench simulation case.

$\omega_{c,\mathrm{lpf}}$	$2000\pi\,\frac{rad}{s}$	$3000\pi\,\frac{rad}{s}$	$4000\pi\,\frac{rad}{s}$	PI BLC
THD	4.28 %	4.17 %	4.16 %	5.43 %

of the approach. This can be explained by the introduced phase-shift, that deteriorates the alignment of the correction term. However, the THD is reduced significantly, at least by 21.2 %, for all $\omega_{c,\mathrm{lpf}}$ values when compared to the PI baseline.

B. Microturbine simulation results and discussion

By extending the control scheme of the simulink example[2] of a power electronically interfaced microturbine with the MFM, we show the transferability of the described control modification. The system under consideration differs from the previous example in the following aspects:

- *Grid parameters*: Nominal frequency is 60 Hz, grid RMS voltage 480 V. Grid connection includes different LC-filter ($L_f = 800\,\mu$H, $C_f = 30\,\mu$F) as well as a transformer.
- *Control system*: Current control loop consists of PID controllers for the filter currents, instead of PI controllers. No cross-coupling network or voltage feedforward are used and outer loops provide the current reference.

Considering the tuning rule described in [10], to tune α s.t. the product $\alpha\,\tilde{u}$ is in the same order of magnitude as $\dot{y}$ has proven useful as a starting point for all considered examples. For the presented simulation experiment, the following parameters are used: $\omega_{c,d} = 3000\pi\frac{\text{rad}}{s}$, $\omega_{c,\,\text{lpf}} = 3400\pi\frac{\text{rad}}{s}$ and $\alpha = 8000$. The control parameters of the baseline PID controller are not changed. Again baseline simulations are performed without the MFM.
Fig. 5 shows the comparison of the current waveform for the PID baseline and enabled MFM. As can be seen from the

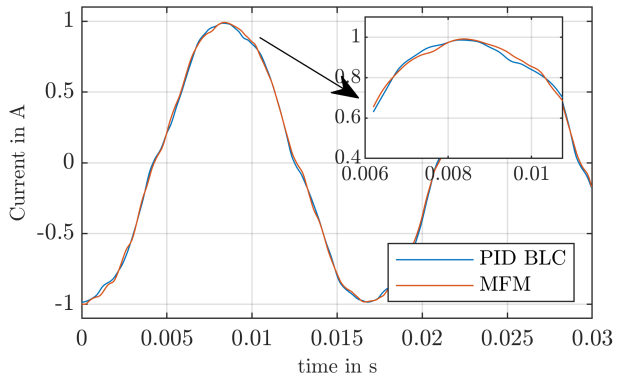

Fig. 5: Comparison of the current waveform for the MT-simulation example with $\alpha = 8000$ and $\omega_{c,\text{lpf}} = 3400\pi\frac{\text{rad}}{s}$.

zoomed plot, the flat peak of the sine wave is improved which is reflected in the improved attenuation of the 5^{th} and 7^{th} harmonic. The total THD value is decreased significantly by $28.4\,\%$ compared to the baseline controller. However, some of the harmonics show an increase, e.g. 6^{th}, 9^{th}, 11^{th}, 14^{th} and 15^{th}, cf. Fig. 6 for a comparison of individual harmonics. This shows that the main goal of the approach, THD reduction, is transferable to similar systems. However, the performance concerning individual harmonics can vary and some further adjustments or tuning might be required to achieve optimal performance.

V. Experimental Results

A. Testbench description and experiment setup

The current controller and MFM are implemented on a digital controller of a grid-tied, three-phase inverter which is connected to the public grid via a transmission line replica, cf. [17] for details on the laboratory. Figure 1 depicts the electric scheme and Figure 7 the hardware setup. Table I summarizes the hardware parameters of the testbench and the

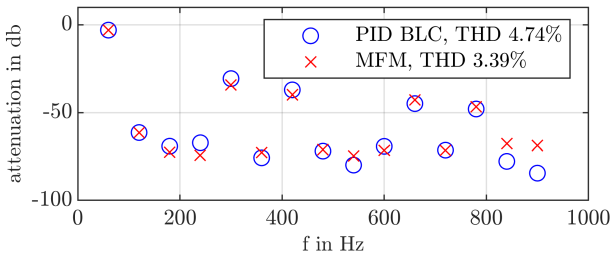

Fig. 6: Comparison of the harmonic powers with enabled MFM, for the MT-simulation example with $\alpha = 8\text{e}3$ and $\omega_{c,\text{lpf}} = 3400\pi\frac{\text{rad}}{s}$.

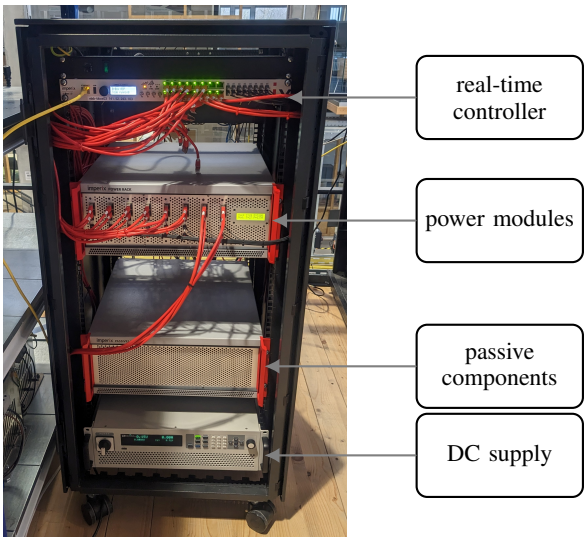

Fig. 7: Image of the hardware setup used for the presented experiments

control parameters are given in Tab. II, if not noted otherwise. The considered experiment procedure is as following:

- Inverter system is connected to the public grid via a series RL-type transmission line replica and the control system is enabled.
- A current setpoint of $i_{\text{dq, d}} = [5 \quad 0]^\top$ is applied. After reaching a steady state, measurement data is collected for a window of 3 s.

B. Experimental results and discussion

First the results of a representative experiment are discussed in detail, afterwards insight in the influence of the tuning of α is given.
Electric current waveform measurement comparing the baseline PI controller results with the enabled MFM are presented in Fig. 8. Again a visible improvement of the peak of the sine wave is shown for enabled MFM. Furthermore, the THD for the presented experiment improves significantly by $13.9\,\%$, from $10.97\,\%$ to $9.44\,\%$. This is a smaller relative improvement than for the simulation example with identical parameters. Possible reasons are the influence of grid voltage harmonics,

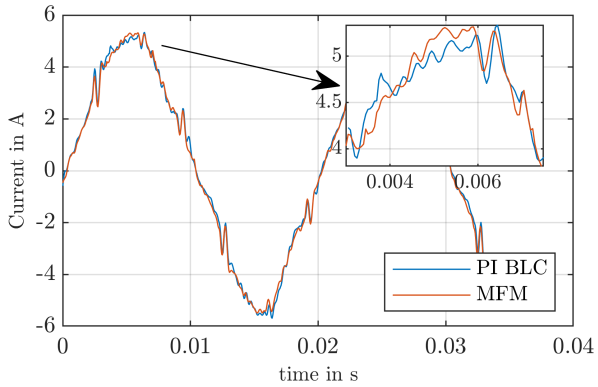

Fig. 8: Comparison of the current waveform with baseline PI controller and enabled MFM. Parameters according to Tab. II

which can propagate through the control system [18], also indicated by the THD value of the capacitor voltages of simulation and experiment: 0.24 % and 1.71 %, respectively. Further, the influence of unmodeled dynamics, such as additional time-delays might deteriorate the performance of the approach.
Figure 9 shows a comparison of the individual harmonics and again we see an improvement for most of the harmonics up

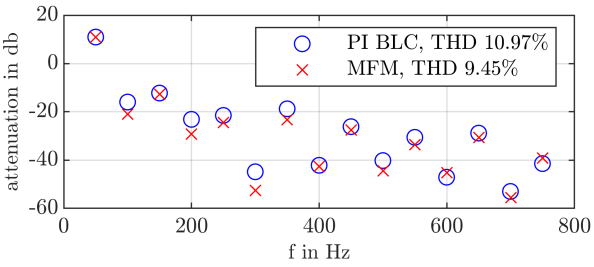

Fig. 9: Comparison of the power of the individual harmonics for the baseline experiment and enabled MFM with $\alpha = 700$, further parameters according to Tab. II.

to the 15^{th} order. Note that the 3^{rd} harmonic is much more pronounced in the hardware measurements compared to the testbench simulation, cf. results shown in Fig. 4.
To discuss the influence of the tuning factor α, several experiments with values ranging from $\alpha = 1400$ to $\alpha = 150$ are conducted, exemplary results are summarized in Tab. IV. The parameter α can be interpreted as a weighting factor between the current derivative and the control input that are used to identify F, where smaller values of α correspond to a larger weight of the current derivative. The results indicate that with the presented implementation of the MFM, there is a trade-off between further improvement of the lower harmonics and increasing the content of the harmonics with order $> 11^{\text{th}}$. A possible explanation for this behavior is the amplified noise contained in the current derivative estimate, that influences the values of the higher order harmonics. Considering the overall THD as an optimality measure, values around $\alpha = 700$ yield the best results for the given setup, with an improvement by 13.9 % compared to the PI controller baseline.

TABLE IV: Influence of α on the THD and individual harmonics. The individual harmonic values are given relative to the PI baseline. Color code: improvement, best shown value and deterioration

THD	PI baseline	$\alpha = 900$	$\alpha = 700$	$\alpha = 500$	$\alpha = 150$
total	10.97 %	9.81 %	9.45 %	9.52 %	11.3 %
2^{nd}	100 %	56.4 %	55.9 %	55.7 %	52.8 %
3^{rd}	100 %	99.3 %	94.5 %	96.6 %	87.2 %
4^{th}	100 %	49.6 %	49.5 %	48.5 %	44.3 %
5^{th}	100 %	79.4 %	71.6 %	71.5 %	68.8 %
6^{th}	100 %	63.6 %	41.1 %	60.9 %	84.7 %
7^{th}	100 %	65.6 %	59.4 %	60.5 %	56.4 %
8^{th}	100 %	94.9 %	93.9 %	85.8 %	57.6 %
9^{th}	100 %	85.1 %	85.4 %	83.6 %	54.4 %
10^{th}	100 %	66.9 %	61.1 %	51.4 %	43.6 %
11^{th}	100 %	79.3 %	70.5 %	74.0 %	52.2 %
$\sum_{12^{\text{th}}}^{50^{\text{th}}}$	100 %	103.1 %	99.9 %	99.0 %	132.1 %

VI. Conclusion

The provided results show that the described model-free control modification is able to reduce the total harmonic distortion (THD) values for the considered simulation examples as well as for the hardware implementation of a grid-tied inverter system. This implementation exhibits a trade-off between further improving the attenuation of lower order harmonics and increasing the harmonic content for higher order harmonics. However, even with the simple implementation and coarse tuning, significant THD improvements are obtained which indicates, that the full potential of the approach is not yet leveraged. As future work, further research with attention to improve the implementation and tuning of the derivative filter and LPF is required to fully exploit the potential of the method.

References

[1] A. Testa, M. F. Akram, R. Burch, G. Carpinelli, G. Chang, V. Dinavahi, C. Hatziadoniu, W. M. Grady, E. Gunther, M. Halpin, P. Lehn, Y. Liu, R. Langella, M. Lowenstein, A. Medina, T. Ortmeyer, S. Ranade, P. Ribeiro, N. Watson, J. Wikston, and W. Xu, "Interharmonics: Theory and modeling," *IEEE Transactions on Power Delivery*, vol. 22, no. 4, pp. 2335–2348, October 2007.

[2] J. Meyer, R. Stiegler, P. Schegner, I. Röder, and A. Belger, "Harmonic resonances in residential low-voltage networks caused by consumer electronics," *CIRED - Open Access Proceedings Journal*, vol. 2017, no. 1, pp. 672–676, October 2017.

[3] D. Chakravorty, J. Meyer, P. Schegner, S. Yanchenko, and M. Schocke, "Impact of modern electronic equipment on the assessment of network harmonic impedance," *IEEE Transactions on Smart Grid*, vol. 8, no. 1, pp. 382–390, January 2017.

[4] F. Möller, J. Meyer, and M. Radauer, "Impact of a high penetration of electric vehicles and photovoltaic inverters on power quality in an urban residential grid part I - unbalance," *Renewable Energy and Power Quality Journal*, no. 14, pp. 817–822, May 2016.

[5] S. Müller, J. Meyer, F. Möller, M. Naumann, and M. Radauer, "Impact of a high penetration of electric vehicles and photovoltaic inverters on power quality in an urban residential grid part II - harmonic distortion," *Renewable Energy and Power Quality Journal*, pp. 823–828, May 2016.
[6] J. Enslin and P. Heskes, "Harmonic interaction between a large number of distributed power inverters and the distribution network," *IEEE Transactions on Power Electronics*, vol. 19, no. 6, pp. 1586–1593, November 2004.
[7] N. Hatziargyriou, J. Milanovic, C. Rahmann, V. Ajjarapu, C. Canizares, I. Erlich, D. Hill, I. Hiskens, I. Kamwa, B. Pal, P. Pourbeik, J. Sanchez-Gasca, A. Stankovic, T. V. Cutsem, V. Vittal, and C. Vournas, "Definition and classification of power system stability – revisited & extended," *IEEE Transactions on Power Systems*, vol. 36, no. 4, pp. 3271–3281, July 2021.
[8] I. Jahn, M. Nahalparvari, S. Norrga, and R. Rogersten, "Moving beyond open-source modelling: why open control and protection software in real converters will be usefull," in *Proceedings of Open Source Modelling and Simulation of Energy Systems (OSMSES)*, pp. 1–6, April 2022.
[9] J. M. Espi, J. Castello, R. García-Gil, G. Garcera, and E. Figueres, "An adaptive robust predictive current control for three-phase grid-connected inverters," *IEEE Transactions on Industrial Electronics*, vol. 58, pp. 3537–3546, August 2011.
[10] M. Fliess and C. Join, "Model-free control," *International Journal of Control*, vol. 86, pp. 2228–2252, December 2013.
[11] Y. Zhang, X. Liu, J. Liu, J. Rodriguez, and C. Garcia, "Model-free predictive current control of power converters based on ultra-local model," in *2020 IEEE International Conference on Industrial Technology (ICIT)*, IEEE, February 2020.
[12] N. Jin, M. Chen, L. Guo, Y. Li, and Y. Chen, "Double-vector model-free predictive control method for voltage source inverter with visualization analysis," *IEEE Transactions on Industrial Electronics*, vol. 69, pp. 10066–10078, October 2022.
[13] J. Rocabert, A. Luna, F. Blaabjerg, and P. Rodríguez, "Control of power converters in AC microgrids," *IEEE Transactions on Power Electronics*, vol. 27, pp. 4734–4749, November 2012.
[14] Y. Levron, J. Belikov, and D. Baimel, "A tutorial on dynamics and control of power systems with distributed and renewable energy sources based on the DQ0 transformation," *Applied Sciences*, vol. 8, p. 1661, September 2018.
[15] A. Othmane, L. Kiltz, and J. Rudolph, "Survey on algebraic numerical differentiation: historical developments, parametrization, examples, and applications," *International Journal of Systems Science*, vol. 53, pp. 1848–1887, February 2022.
[16] IEEE Harmonics Working Group, "IEEE recommended practice and requirements for harmonic control in electric power systems," June 2014.
[17] F. Wiegel, J. Wachter, M. Kyesswa, R. Mikut, S. Waczowicz, and V. Hagenmeyer, "Smart energy system control laboratory – a fully-automated and user-oriented research infrastructure for controlling and operating smart energy systems," *at - Automatisierungstechnik*, vol. 70, pp. 1116–1133, December 2022.
[18] X. Wang and F. Blaabjerg, "Harmonic stability in power electronic-based power systems: Concept, modeling, and analysis," *IEEE Transactions on Smart Grid*, vol. 10, no. 3, pp. 2858–2870, May 2019.